Supplemental Material for: Detection of Molecular Changes with Nitrogen-Vacancy Centers and Electron-Spin Labels

C. Munuera-Javaloy,[1] R. Puebla,[2,3] B. D'Anjou,[4] M. B. Plenio,[4] and J. Casanova[1,5]

[1]*Department of Physical Chemistry, University of the Basque Country UPV/EHU, Apartado 644, 48080 Bilbao, Spain*
[2]*Instituto de Física Fundamental, IFF-CSIC, Calle Serrano 113b, 28006 Madrid, Spain*
[3]*Centre for Theoretical Atomic, Molecular, and Optical Physics, School of Mathematics and Physics, Queen's University, Belfast BT7 1NN, United Kingdom*
[4]*Institut für Theoretische Physik and IQST, Universität Ulm, Albert-Einstein-Allee 11, D-89069 Ulm, Germany*
[5]*IKERBASQUE, Basque Foundation for Science, Plaza Euskadi 5, 48009 Bilbao, Spain*

I. NV-LABELS HAMILTONIAN

In the following, we derive Eq. (1) of the main text. We start with the Hamiltonian for a driven NV center interacting with two driven nitroxide electron-spin labels. The full Hamiltonian is

$$H = D\,(S^z)^2 + B^z|\gamma_e|S^z + H_{n_1} + H_{n_2} + \sum_{i=1,2} H_{\mathrm{NV}-n_i} + H_{ee} + \sqrt{2}\Omega_{\mathrm{MW}}S^x\cos(\omega_{\mathrm{MW}}t) + 2\Omega_{\mathrm{RF}}\left(J_1^x + J_2^x\right)\cos(\omega_{\mathrm{RF}}t). \tag{S1}$$

Here, $D = 2\pi \times 2.87$ GHz is the zero-field splitting of the NV center, $|\gamma_e| = 2\pi \times 28$ MHz/mT is the electron gyromagnetic ratio, $H_{\mathrm{NV}-n_i} = \frac{\mu_0\gamma_e^2\hbar}{4\pi d_i^3}\left[\vec{S}\cdot\vec{J}_i - \frac{3\left(\vec{S}\cdot\vec{r}_i\right)\left(\vec{J}_i\cdot\vec{r}_i\right)}{d_i^2}\right]$ is the dipolar interaction between the NV and the ith label electron, and $H_{ee} = \frac{\mu_0\gamma_e^2\hbar}{4\pi d_{12}^3}\left[\vec{J}_1\cdot\vec{J}_2 - \frac{3\left(\vec{J}_1\cdot\vec{r}_{12}\right)\left(\vec{J}_2\cdot\vec{r}_{12}\right)}{d_{12}^2}\right]$ is the dipolar interaction between label electrons. In these equations, $\vec{r}_i$ is the vector joining the NV with the ith label, $\vec{r}_{12} = \vec{r}_1 - \vec{r}_2$ is the relative vector that connects the two labels, $d_i = |\vec{r}_i|$, and $d_{12} = |\vec{r}_{12}|$. The last two terms on the right hand side of Eq. (S1) are the MW and RF driving terms, respectively. We move to the interaction picture with respect to $H_0 = D\,(S^z)^2 + |\gamma_e|B^zS^z = \omega_+|1\rangle\langle 1| + \omega_-|-1\rangle\langle -1|$, with $\omega_\pm = D \pm |\gamma_e|B^z$. In addition, we set the MW field on resonance with the $0 \leftrightarrow 1$ NV transition ($\omega_{\mathrm{MW}} = \omega_+$). In the interaction picture, the Hamiltonian takes the form

$$H_I = H_{n_1} + H_{n_2} + S^z\left(\vec{a}_1\cdot\vec{J}_1 + \vec{a}_2\cdot\vec{J}_2\right) + H_{ee} + \frac{\Omega_{\mathrm{MW}}}{2}\left(|0\rangle\langle 1| + |1\rangle\langle 0|\right) + 2\Omega_{\mathrm{RF}}\left(J_1^x + J_2^x\right)\cos(\omega_{\mathrm{RF}}t). \tag{S2}$$

Note that we substituted $H_{\mathrm{NV}-n_i} \to S^z\vec{a}_i\cdot\vec{J}_i$, with $\vec{a}_i = \frac{\mu_0\gamma_e^2\hbar}{4\pi d_i^3}\left[\hat{z} - \frac{3r_i^z\vec{r}_i}{d_i^2}\right]$. This is justifiable since the strength of the interaction between the NV and labels is much smaller than the transition energies of the NV. Therefore, the terms proportional to $S^{x,y}$ can be neglected in the RWA.

We initialize the NV in the $m_s = 1, 0$ manifold. Moreover, the Hamiltonian does not contain terms that can significantly populate the $m_s = -1$ subspace. Consequently, we can project the Hamiltonian on the $m_s = 1, 0$ manifold and treat the NV as a two-level system. The resulting Hamiltonian is

$$H_I = H_{n_1} + H_{n_2} + \frac{\mathbb{I} + \sigma^z}{2}\left(\vec{a}_1\cdot\vec{J}_1 + \vec{a}_2\cdot\vec{J}_2\right) + H_{ee} + \frac{\Omega_{\mathrm{MW}}}{2}\sigma^x + 2\Omega_{\mathrm{RF}}\left(J_1^x + J_2^x\right)\cos(\omega_{\mathrm{RF}}t), \tag{S3}$$

where $\mathbb{I} = |1\rangle\langle 1| + |0\rangle\langle 0|$, $\sigma^z = |1\rangle\langle 1| - |0\rangle\langle 0|$, and $\sigma^x = |1\rangle\langle 0| + |0\rangle\langle 1|$.

The next approximation consists in removing the counter-rotating terms in H_{ee}. These are terms of the form $J_1^+J_2^+$ and $J_1^-J_2^-$ that precess under the externally applied magnetic field B^z. They can be neglected in the RWA since the strength of the coupling between label electrons is much smaller than their Zeeman energy. Under this assumption, H_{ee} simplifies to

$$H_{ee} \approx \frac{\mu_0\gamma_e^2\hbar}{4\pi d_{12}^3}\left[1 - 3\left(\frac{r_{12}^z}{d_{12}}\right)^2\right]\left[J_1^zJ_2^z - \frac{1}{4}\left(J_1^+J_2^- + J_1^-J_2^+\right)\right], \tag{S4}$$

with $J_i^\pm = J_i^x \pm iJ_i^y$ and $g_{12} = \frac{\mu_0\gamma_e^2\hbar}{4\pi d_{12}^3}\left[1 - 3\left(\frac{r_{12}^z}{d_{12}}\right)^2\right]$. Combining the above approximations leads to Eq. (1) of the main text.

II. SIMPLIFIED DYNAMICS OF THE NITROXIDE LABELS

In this section, we develop a simplified model of electron-nucleus dynamics within each nitroxide label. Our approach is based on a perturbative treatment of the nitroxide nuclear degrees of freedom that are orthogonal to the z direction, i.e., the direction of

the external magnetic field. We first introduce the rotation matrices used to relate the laboratory axes and the nitroxide principal axes, namely,

$$R^y(\theta) = \begin{pmatrix} \cos\theta & 0 & \sin\theta \\ 0 & 1 & 0 \\ -\sin\theta & 0 & \cos\theta \end{pmatrix}, \quad R^z(\varphi) = \begin{pmatrix} \cos\varphi & -\sin\varphi & 0 \\ \sin\varphi & \cos\varphi & 0 \\ 0 & 0 & 1 \end{pmatrix}. \tag{S5}$$

The two frames are related via the combined rotation $R(\theta,\varphi) = R^z(\varphi)R^y(\theta)$. In particular, a tensor $\mathbb{O}^{(P)}$ defined with respect to the nitroxide principal axes takes the form $\mathbb{O} = R(\theta,\varphi)\mathbb{O}^{(P)}R(\theta,\varphi)^\intercal$ in the laboratory frame. For instance, consider the nitroxide Hamiltonians [Eq. (2) of the main text]. In the present analysis, we ignore the quadrupolar and nuclear Larmor terms since they are small and do not contribute significantly to the dynamics. The validity of this last assumption was confirmed by our detailed numerical simulations. With this assumption, the nitroxide Hamiltonians expressed in the laboratory frame become

$$H_{n_i} \approx \mu_B B^z \hat{z}\cdot\mathbb{G}_i\cdot\vec{J}_i + \vec{J}_i\cdot\mathbb{A}_i\cdot\vec{I}_i = \mu_B B^z\hat{z}\cdot R(\theta_i,\varphi_i)\mathbb{G}_i^{(P)}R(\theta_i,\varphi_i)^\intercal\cdot\vec{J}_i + \vec{J}_i\cdot R(\theta_i,\varphi_i)\mathbb{A}_i^{(P)}R(\theta_i,\varphi_i)^\intercal\cdot\vec{I}_i. \tag{S6}$$

Due to the symmetry of the $\mathbb{G}_i^{(P)}$ and $\mathbb{A}_i^{(P)}$ tensors ($G^x \approx G^y \approx 2.007$ and $A^x \approx A^y \approx 2\pi\times 14$ MHz) we can set $\varphi_i = 0$ without loss of generality. We find

$$\begin{aligned} H_{n_i} =& \frac{\mu_B B^z}{2}(G^\parallel - G^\perp)\sin(2\theta_i)J_i^x + \frac{\mu_B B^z}{2}\left[(G^\parallel - G^\perp)\cos(2\theta_i) + G^\perp + G^\parallel\right]J_i^z \\ &+ \frac{A^\parallel - A^\perp}{2}\sin(2\theta_i)J_i^zI_i^x + \left(\frac{A^\parallel + A^\perp}{2} + \frac{A^\parallel - A^\perp}{2}\cos(2\theta_i)\right)J_i^zI_i^z \\ &+ A^\perp J_i^yI_i^y + \left(\frac{A^\parallel + A^\perp}{2} - \frac{A^\parallel - A^\perp}{2}\cos(2\theta_i)\right)J_i^xI_i^x + \frac{A^\parallel - A^\perp}{2}\sin(2\theta_i)J_i^xI_i^z. \end{aligned} \tag{S7}$$

A. Simplified dynamics of a nitroxide label hosting ^{14}N

As a first approximation, we keep only the terms proportional to J_i^z in Eq. (S7) . This is a reasonable first approximation since the hyperfine interaction is typically smaller than the electronic Zeeman energy. The resulting Hamiltonian is

$$\begin{aligned} H_{\text{diag}} &= \frac{\mu_B B^z}{2}\left[(G^\parallel - G^\perp)\cos(2\theta_i) + G^\perp + G^\parallel\right]J_i^z + \left(\frac{A^\parallel + A^\perp}{2} + \frac{A^\parallel - A^\perp}{2}\cos(2\theta_i)\right)J_i^zI_i^z + \frac{A^\parallel - A^\perp}{2}\sin(2\theta_i)J_i^zI_i^x \\ &= \mu_B B^z G(\theta_i)J_i^z + \left[\left(\frac{A^\perp + A^\parallel}{2} + \frac{A^\parallel - A^\perp}{2}\cos(2\theta_i)\right)I_i^z + \frac{A^\parallel - A^\perp}{2}\sin(2\theta_i)I_i^x\right]J_i^z, \end{aligned} \tag{S8}$$

where $G(\theta) = \frac{1}{2}\left[(G^\parallel - G^\perp)\cos(2\theta) + G^\perp + G^\parallel\right]$. To find the shifts on J_i^z associated to specific nuclear spin states, we diagonalize the term

$$\left(\frac{A^\perp + A^\parallel}{2} + \frac{A^\parallel - A^\perp}{2}\cos(2\theta_i)\right)I_i^z + \frac{A^\parallel - A^\perp}{2}\sin(2\theta_i)I_i^x. \tag{S9}$$

Since ^{14}N is a spin-1 particle, diagonalization leads to three nuclear eigenstates $|\widetilde{0}\rangle$, $|\widetilde{1}\rangle$, and $|-\widetilde{1}\rangle$. The states have eigenenergies

$$\begin{aligned} \omega_0^i &= 0, \\ \omega_1^i &= \frac{1}{\sqrt{2}}\sqrt{\left[(A^\parallel)^2 - (A^\perp)^2\right]\cos(2\theta_i) + (A^\perp)^2 + (A^\parallel)^2}, \\ \omega_{-1}^i &= -\frac{1}{\sqrt{2}}\sqrt{\left[(A^\parallel)^2 - (A^\perp)^2\right]\cos(2\theta_i) + (A^\perp)^2 + (A^\parallel)^2}. \end{aligned} \tag{S10}$$

Thus, our leading approximation for the nitroxide Hamiltonian is

$$H_{n_i} \approx \left[E_1^i|\widetilde{1}\rangle\langle\widetilde{1}| + E_0^i|\widetilde{0}\rangle\langle\widetilde{0}| + E_{-1}^i|-\widetilde{1}\rangle\langle-\widetilde{1}|\right]J_i^z, \tag{S11}$$

where

$$\begin{aligned} E_0^i &= \mu_B B^z G(\theta_i), \\ E_1^i &= \mu_B B^z G(\theta_i) + \frac{1}{\sqrt{2}}\sqrt{\left[(A^\parallel)^2 - (A^\perp)^2\right]\cos(2\theta_i) + (A^\perp)^2 + (A^\parallel)^2}, \\ E_{-1}^i &= \mu_B B^z G(\theta_i) - \frac{1}{\sqrt{2}}\sqrt{\left[(A^\parallel)^2 - (A^\perp)^2\right]\cos(2\theta_i) + (A^\perp)^2 + (A^\parallel)^2}. \end{aligned} \tag{S12}$$

The above expressions reveal the existence of three energy-transition branches. There is one central branch with energy $\mu_B B^z G(\theta_i)$. The other two branches are shifted from the central branch by $\pm\left|\frac{1}{\sqrt{2}}\sqrt{[(A^{\parallel})^2-(A^{\perp})^2]\cos(2\theta_i)+(A^{\perp})^2+(A^{\parallel})^2}\right|$. A full energy diagram is given in Fig. S1. Note that for moderate magnetic fields, E_0^i depends much more weakly than $E_{1,-1}^i$ on

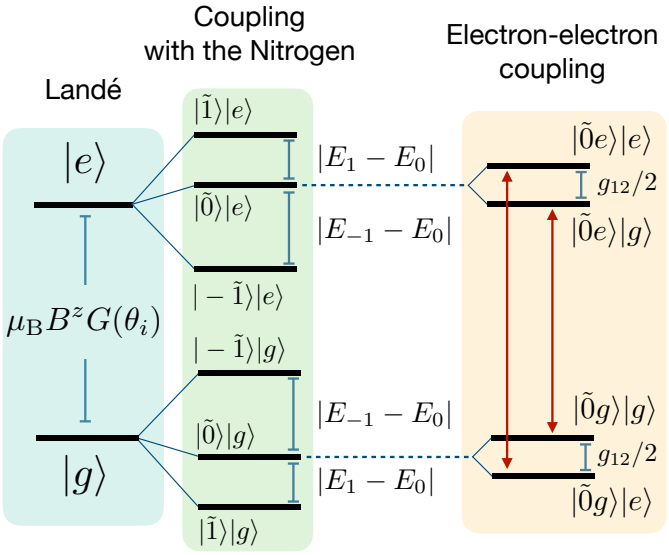

FIG. S1. Energy diagram of a nitroxide label hosting a ^{14}N. A magnetic field B^z is applied along the laboratory z axis, leading to a Landé splitting of the electronic states (blue panel). The hyperfine coupling between the label electron and the nitrogen then splits the energy levels (green panel). Finally, each level is further split in two by the coupling between label electrons (yellow panel). The red arrows in the yellow panel indicate the transitions targeted by our protocol.

the nitroxide azimuth θ_i since the Landé tensor is almost isotropic, $G^{\parallel}\simeq G^{\perp}$, while the hyperfine tensor is strongly anisotropic, $A^{\parallel}\neq A^{\perp}$. Thus, the central branch is particularly important since it can be robust against molecular tumbling (i.e., robust against changes in θ_i). Note, however, that the dependence of E_0^i on θ_i due to the small anistropy of the Landé tensor can become significant if the magnetic field becomes too large. At low magnetic fields, the above approximation starts to break down. We now investigate the leading correction to the central branch E_0^i due to the hyperfine interaction in that regime. This correction arises from the nondiagonal terms in Eq. (S7), i.e., the terms proportional to $J_i^{x,y}$. We first rewrite the nondiagonal terms in Eq. (S7) as

$$V=\alpha_i J_i^x+\beta_i J_i^y, \tag{S13}$$

where

$$\alpha_i=\left(A^{\perp}\cos^2(\theta_i)+A^{\parallel}\sin^2(\theta_i)\right)I^x+\left(A^{\parallel}-A^{\perp}\right)I^z\cos(\theta_i)\sin(\theta_i),\quad \beta_i=A^{\perp}I^y. \tag{S14}$$

We find the second-order correction due to V by performing operator perturbation theory. More precisely, we move to a rotating frame with respect to $\mu_B B^z G(\theta_i)J_i^z$ and find the effective contribution of V by keeping time-independent terms in its Dyson series (expanded up to second order). This leads to an effective interaction $\frac{(\alpha_i-i\beta_i)(\alpha_i+i\beta_i)}{2\mu_B B^z G(\theta_i)}J_i^z$. Projecting this expression onto the $|\widetilde{0}\rangle$ subspace gives the leading correction to E_0^i,

$$\frac{1}{2\mu_B B^z G(\theta_i)}\frac{2(A^{\perp}A^{\parallel})^2+\left[(A^{\perp})^4-(A^{\perp}A^{\parallel})^2\right]\sin^2(\theta_i)}{(A^{\perp})^2\sin^2(\theta_i)+(A^{\parallel})^2\cos^2(\theta_i)}. \tag{S15}$$

This expression shows that the anisotropy of the hyperfine tensor can lead to a strong dependence of E_0^i on θ_i when the magnetic field becomes small enough to be comparable to the hyperfine coupling. From the above arguments, we therefore expect that there exists an optimum magnetic field strength where the central branch is most robust to variations in the azimuth θ_i. This is illustrated in Fig. S2.

In summary, we write the nitroxide Hamiltonian as

$$H_{n_i}\approx\left[E_1^i|\widetilde{1}\rangle\langle\widetilde{1}|_i+E_0^i|\widetilde{0}\rangle\langle\widetilde{0}|_i+E_{-1}^i|-\widetilde{1}\rangle\langle-\widetilde{1}|_i\right]J_i^z, \tag{S16}$$

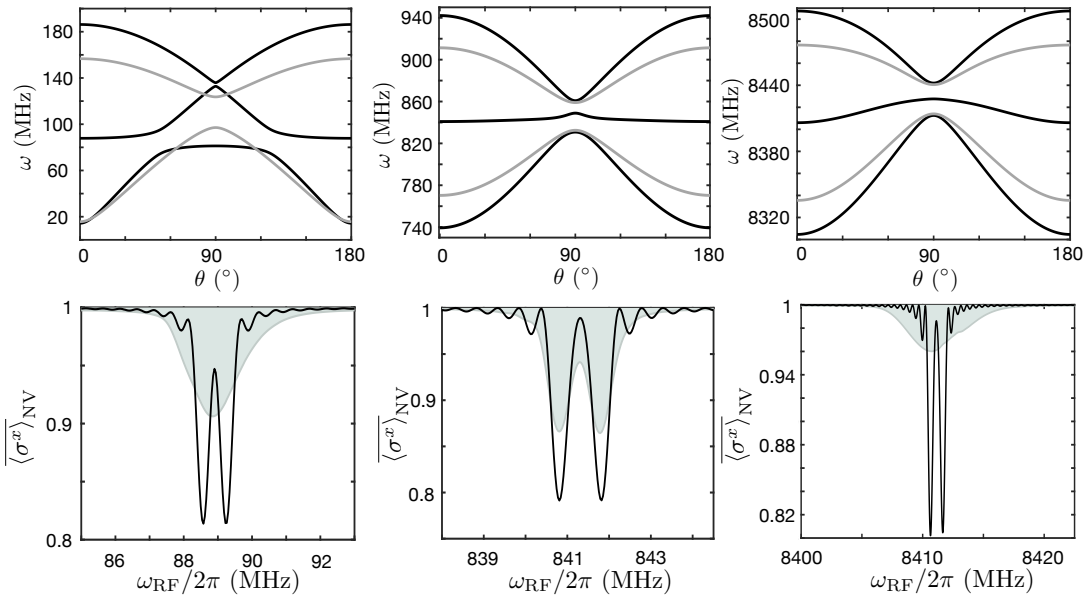

FIG. S2. (Top panels) Energy-transition branches of a nitroxide as a function of its azimuth angle θ for B = 3, 30 and 300 mT (left to right). Solid black (grey) lines correspond to a nitroxide hosting ^{14}N (^{15}N). All branches are obtained by diagonalizing Eq. (2) of the main text. (Bottom panels) Numerical simulation of the average NV spectrum $\overline{\langle\sigma^x\rangle}_{\rm NV}$ for the same magnetic fields as in the top panels. All simulations are performed by unitary propagation of Eq. (1) of the main text and using the full nitroxide Hamiltonian, Eq. (2). We show the spectrum for an equilibrium azimuth $\theta_{\rm eq} = 30^\circ$ (black lines) and the spectra averaged over a Gaussian distribution of angles centered at $\theta_{\rm eq}$ and with standard deviation $\sigma_\theta = 6.25^\circ$ (shaded areas). At intermediate magnetic fields, the spectrum is resilient to tumbling due to a weak dependence of the central branch E_0 on θ.

with

$$E_0^i = \mu_B B^z G(\theta_i) + \frac{1}{2\mu_B B^z G(\theta_i)} \frac{2(A^\perp A^\parallel)^2 + \left[(A^\perp)^4 - (A^\perp A^\parallel)^2\right]\sin^2(\theta_i)}{(A^\perp)^2\sin^2(\theta_i) + (A^\parallel)^2\cos^2(\theta_i)},$$
$$E_1^i = \mu_B B^z G(\theta_i) + \frac{1}{\sqrt{2}}\sqrt{\left[(A^\parallel)^2 - (A^\perp)^2\right]\cos(2\theta_i) + (A^\perp)^2 + (A^\parallel)^2},$$
$$E_{-1}^i = \mu_B B^z G(\theta_i) - \frac{1}{\sqrt{2}}\sqrt{\left[(A^\parallel)^2 - (A^\perp)^2\right]\cos(2\theta_i) + (A^\perp)^2 + (A^\parallel)^2}.$$

B. Simplified dynamics of a nitroxide label hosting ^{15}N

For a ^{15}N, (i.e., a spin-1/2 particle) the diagonalization of Eq. (S9) yields two nitrogen eigenstates $|\widetilde{1/2}\rangle$ and $|-\widetilde{1/2}\rangle$ with eigenergies

$$E_{1/2,-1/2}^i = \mu_B B^z G(\theta_i) \pm \frac{\sqrt{(A^\perp)^2 + (A^\parallel)^2 + \left[(A^\parallel)^2 - (A^\perp)^2\right]\cos(2\theta_i)}}{2\sqrt{2}}. \tag{S17}$$

III. DETAILS OF THE NUMERICAL SIMULATIONS

A. Dissipative model

Our detailed numerical simulations account for decoherence in ambient conditions using a Lindblad master equation of the form

$$\dot{\rho} = -i\left[H,\rho\right] + \frac{1}{2T_2}\left(\sigma^z\rho\sigma^z - \rho\right) + \sum_{i=1,2}\left[\Gamma(\bar{n}+1)\left(J_i^-\rho J_i^+ - \frac{1}{2}J_i^+J_i^-\rho - \frac{1}{2}\rho J_i^+J_i^-\right) + \Gamma\bar{n}\left(J_i^+\rho J_i^- - \frac{1}{2}J_i^-J_i^+\rho - \frac{1}{2}\rho J_i^-J_i^+\right)\right]. \tag{S18}$$

Here, $T_2 = 20\ \mu$s is the NV coherence time for an NV depth of 4 nm [S1], $\Gamma \approx 2\pi \times 2.68$ Hz is the relaxation rate of the label electrons, and $\bar{n} = 1/\left[\exp\left(\hbar\gamma_e B^z/k_B T\right) - 1\right]$ is the thermal occupation of a bosonic thermal bath of temperature T that generates electronic transitions. For the magnetic field $B^z = 30$ mT and the temperature $T = 300$ K used in our simulations, this corresponds to an electronic relaxation time $T_1 = 1/\left[(2\bar{n}+1)\Gamma\right] \approx 4\ \mu$s [S1]. The coherent part of the evolution in the presence of driving is described by the Hamiltonian

$$H = \frac{\Omega_{\rm MW}}{2}\sigma^x + g_{12}\left[J_1^zJ_2^z - \frac{1}{4}\left(J_1^+J_2^- + J_1^-J_2^+\right)\right] + \sum_{i=1,2}\left[\frac{1}{2}\left(\mathbb{I}+\sigma^z\right)\vec{a}_i\cdot\vec{J}_i + \mu_B B^z\hat{z}\cdot\mathbb{G}_i\cdot\vec{J}_i + \gamma_N B^z I_i^z + \vec{I}_i\cdot\mathbb{Q}_i\cdot\vec{I}_i + \vec{J}_i\cdot\mathbb{A}_i\cdot\vec{I}_i + 2\Omega_{\rm RF}J_i^x\cos(\omega_{\rm RF}t)\right]. \tag{S19}$$

The above model was previously used to accurately describe the experimental results of Ref. [S1].

B. Molecular tumbling

Figure S3 depicts the effect of molecular tumbling on the orientations and positions of the nitroxides before rotation and after rotation. For all simulations, the molecule rotates around an axis that is parallel to the laboratory x axis and that contains the point $\vec{r}_0 = (3,0,6)$ nm. For the simulations of Fig. 3(a,d), the equilibrium positions of the two nitroxides are $\vec{r}_{1,\rm eq} = (-2.10, 2.17, 6.24)$ nm and $\vec{r}_{2,\rm eq} = (0.4, 0.3, 7.3)$ nm and their equilibrium orientations are $(\theta_{1,\rm eq},\varphi_{1,\rm eq}) = (11.46, -91.67)^\circ$ and $(\theta_{2,\rm eq},\varphi_{2,\rm eq}) = (91.67, 154.70)^\circ$. For the simulation of Fig. 3(b), the equilibrium positions are $\vec{r}_{1,\rm eq} = (-2.10, 2.17, 6.24)$ nm and $\vec{r}_{2,\rm eq} = (0.89, 0.39, 8.27)$ nm and the equilibrium orientations are $(\theta_{1,\rm eq},\varphi_{1,\rm eq}) = (11.46, -91.67)^\circ$ and $(\theta_{2,\rm eq},\varphi_{2,\rm eq}) = (91.67, 154.70)^\circ$. For the simulation of Fig. 3(c), the equilibrium positions are $\vec{r}_{1,\rm eq} = (-2.10, 2.17, 6.24)$ nm and $\vec{r}_{2,\rm eq} = (0.4, 0.3, 7.3)$ nm and the equilibrium orientations are $(\theta_{1,\rm eq},\varphi_{1,\rm eq}) = (63.03, -91.67)^\circ$ and $(\theta_{2,\rm eq},\varphi_{2,\rm eq}) = (51.57, 154.70)^\circ$. All positions are measured with respect to an origin located at the NV center. The average spectrum $\overline{\langle\sigma^x\rangle}_{\rm NV}$ is obtained by averaging spectra assuming that the rotation angle δ follows a Gaussian distribution with zero mean and standard deviation 6.25°. Finally, note that the molecular tumbling has a correlation time of ∼1 ms for typical proteins at room temperature [S1]. Since the NV signal must be averaged over several seconds (see Sec. III D), all tumbling configurations are averaged over in the course of the experiment

C. Inference model

In this section, we motivate the expression used for Bayesian parameter inference in the main text. We make the following simplifying assumptions:

1. The system is simplified to a single NV interacting with a single target nitroxide (^{14}N) with orientation (θ,φ). The only role of the other nitroxide is to introduce an energy shift $\pm g_{12}(\beta)/2$ on the target nitroxide depending on its state. Here, $g_{12}(\beta) \propto d_{12}^{-3}(1 - 3\cos^2\beta)$ is the dipole-dipole coupling and β is the angle between the magnetic field and the vector $\vec{r}_{12}$ joining the nitroxides.

2. The longitudinal coupling a^z between the NV and target nitroxide stays approximately constant during molecular tumbling. This is a reasonable approximation for small molecular tumbling angles.

3. The driving frequency $\omega_{\rm RF}$ is close to resonance with the $E_0(\theta)$ energy-transition branch of the target nitroxide and far off resonance with the other branches. Therefore, non-trivial evolution of the target nitroxide occurs only for nuclear eigenstate $|\widetilde{0}\rangle$.

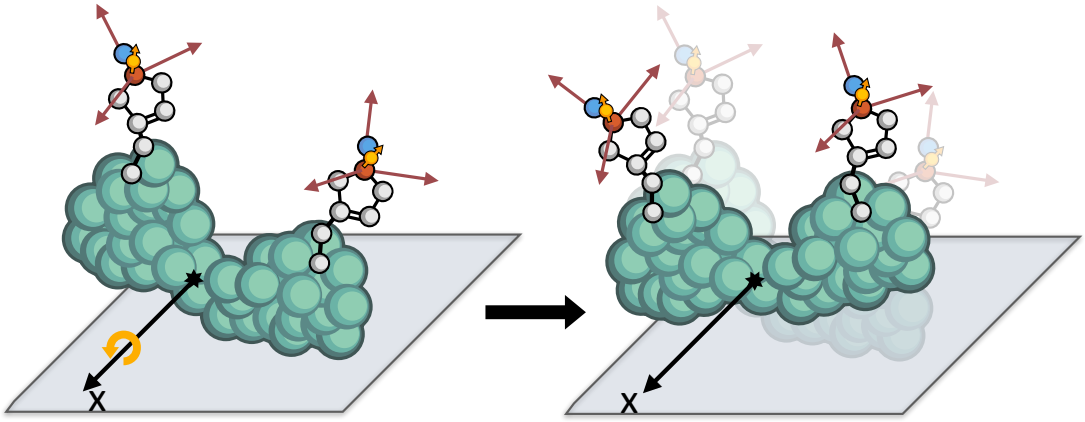

FIG. S3. Starting from an initial configuration (left), the molecule is slightly rotated around an axis parallel to the laboratory x axis (right). In the right panel, the transparent image shows the initial configuration for better comparison.

4. The π-pulse on the NV is simply described by the action of the operator $-i\sigma^x$, i.e., the interaction between the NV and label electrons during irradiation can be neglected.

With these assumptions, the Hamiltonian of the target nitroxide during free evolution is $H_{\text{free},\pm} = \left\{\left[E_0(\theta) - \omega_{\text{RF}} \pm \frac{g_{12}(\beta)}{2}\right] J^z + \frac{a^z}{2}\sigma^z J^z\right\} \otimes |\widetilde{0}\rangle\langle\widetilde{0}|$. Similarly, the Hamiltonian of the target nitroxide during irradiation is $H_{\text{pulse},\pm} = \left\{\left[E_0(\theta) - \omega_{\text{RF}} \pm \frac{g_{12}(\beta)}{2}\right] J^z + \Omega_{\text{RF}} J^x\right\} \otimes |\widetilde{0}\rangle\langle\widetilde{0}|$. In these expressions, the index $\pm$ labels the states of the other nitroxide electron. For coherent dynamics, these Hamiltonians yield the propagator $U_\pm = e^{-iH_{\text{free},\pm}\tau_{\text{free}}} e^{-iH_{\text{pulse},\pm}\frac{\pi}{\Omega_{\text{RF}}}} (-i\sigma^x) e^{-iH_{\text{free},\pm}\tau_{\text{free}}}$. We assume an initial state $\rho = |+\rangle\langle+| \otimes \frac{\mathbb{I}}{2} \otimes \frac{\mathbb{I}}{3}$, i.e., the target nitroxide is in a fully mixed state. We also assume that the other nitroxide is in a fully mixed state so that the evolutions $U_\pm$ have equal probability. With these initial conditions, we find that the spectrum $\mathcal{S}(\omega_{\text{RF}}, \theta, \beta) = \langle\sigma^x\rangle_{\text{NV}}$ has the form

$$\mathcal{S}(\omega_{\text{RF}}, \theta, \beta) \approx \sum_{s=+,-} \frac{1}{2}\text{Tr}\left(U_s \rho U_s^\dagger \sigma^x\right) = \mathcal{S}_0 - \sum_{s=+,-} C_s \left[\frac{\Omega_{\text{RF}}}{\Omega_s(\omega_{\text{RF}}, \theta, \beta)}\right]^2 \sin^2\left[\frac{\pi}{2}\frac{\Omega_s(\omega_{\text{RF}}, \theta, \beta)}{\Omega_{\text{RF}}}\right], \tag{S20}$$

where $\Omega_\pm^2(\omega_{\text{RF}}, \theta, \beta) = \Omega_{\text{RF}}^2 + [\omega_{\text{RF}} - E_0(\theta) \pm g_{12}(\beta)/2]^2$, $\mathcal{S}_0 = 1$, and $C_s = \frac{1}{6}\sin^2\left(\frac{a^z\tau_{\text{free}}}{2}\right)$. For a fixed value of τ_{free}, we expect the main effect of dissipation to be two-fold. First, NV decoherence can modify the baseline NV response $\mathcal{S}_0$ when the drive is off-resonant. Second, NV decoherence and relaxation of the nitroxide electrons can reduce the contrast C_s in a way that may depend on $s = \pm$. Therefore, we leave $\mathcal{S}_0$, C_+, and C_- as adjustable parameters for the dissipative model. In the presence of molecular tumbling, the average spectrum $\overline{\mathcal{S}}(\omega_{\text{RF}})$ is obtained by averaging Eq. (S20) over a suitable distribution of the tumbling angle δ, with the angles θ and β both depending on δ. For tumbling by an angle δ around an axis parallel to the laboratory x axis (see Fig. S3), the azimuth angle θ of the target nitroxide is related to δ by

$$\theta(\delta) = \arccos\left[\cos(\delta)\cos(\theta_{\text{eq}}) + \sin(\delta)\sin(\theta_{\text{eq}})\sin(\varphi_{\text{eq}})\right], \tag{S21}$$

where $(\theta_{\text{eq}}, \varphi_{\text{eq}})$ is the equilibrium orientation of the target nitroxide. Moreover, the dependence of the angle β on the tumbling angle δ is described by the expression $\cos^2[\beta(\delta)] = A_\beta^2 \cos^2(\delta + \phi_\beta)$, where A_β and ϕ_β are parameters capturing the orientation of $\vec{r}_{12}$ in the $x-y$ plane. Using these relations, the average spectrum $\overline{\mathcal{S}}(\omega_{\text{RF}})$ is obtained by numerically averaging $\mathcal{S}[\omega_{\text{RF}}, \theta(\delta), \beta(\delta)]$ over δ assuming that δ is Gaussian-distributed with unknown standard deviation σ_δ. When trying to infer d_{12}, there are nine adjustable parameters in total. We assume that $\mathcal{S}_0$ is calibrated and known. The remaining eight adjustable parameters are $\mathbf{V} = \{C_+, C_-, \theta_{\text{eq}}, \varphi_{\text{eq}}, A_\beta, \phi_\beta, d_{12}, \sigma_\delta\}$.

D. Inference of the distance between nitroxide electron-spin labels

We now describe how to infer system parameters from the simplified model discussed in Sec. III C. We first simulate the acquisition of experimental data from a spectrum obtained numerically using Eq. (S19). Here, we use the spectrum of Fig. 3(a) in the main text. The data has the form $\mathbf{X} = \{X_1, \ldots, X_M\}$, where X_j is an estimate of the probability $\mathcal{P}_+ = \left(1 + \overline{\langle\sigma^x\rangle}_{\text{NV}}\right)/2$ of the NV occupying the +1 eigenstate of σ^x when the target nitroxide is driven at frequency $\omega_{\text{RF},j}$. Assuming ideal NV measurements,

the simulated values of X_j are drawn independently from a Binomial distribution, $X_j \sim B(N_m, \mathcal{P}_+)/N_m$. Fig. S4(a) shows an example simulated dataset $\mathbf{X}$. The "true" spectrum $\mathcal{P}_+ = \left(1 + \overline{\langle\sigma^x\rangle}_{\rm NV}\right)/2$ and the approximate spectrum $\mathcal{P}_+ = \left(1 + \overline{\mathcal{S}}(\omega_{\rm RF})\right)/2$ are also shown for comparison. The values of $\theta_{\rm eq}, \varphi_{\rm eq}, A_\beta, \phi_\beta, d_{12}$ and σ_δ used to plot the approximate spectrum are the same as for the "true" spectrum, while the contrasts $C_\pm$ and baseline $\mathcal{S}_0$ are adjusted to fit the "true" spectrum. The two spectra are in good agreement, suggesting that our simplified model can be safely used to infer the system parameters $\mathbf{V}$. To infer the parameters, we assume that X_j is Gaussian distributed with mean $\left(1 + \overline{\mathcal{S}}(\omega_{{\rm RF},j})\right)/2$ and variance $\sigma_m^2 = \left(1 - \overline{\mathcal{S}}(\omega_{{\rm RF},j})^2\right)/4N_m$. The Gaussian approximation is justifiable when the number N_m of measurements per frequency is large. Since $\overline{\mathcal{S}} \approx 0.34$ at all frequencies for the spectrum of Fig. 3(a), we fix σ_m^2 to a constant value $\sigma_m^2 \approx 0.22/N_m$. In addition, we assume a uniform prior for $\mathbf{V}$. The posterior distribution $L(\mathbf{V}|\mathbf{X})$ is then sampled using a standard Metropolis algorithm [S2]. Fig. S4(b) shows an example Markov chain for the parameters d_{12}, C_+, and C_- (the contrasts $C_\pm$ are multiplied by a factor 10 for easier viewing). The resulting marginal posterior for d_{12} is shown in Fig. 4(d) of the main text. For reference, the marginal posterior of $|g_{12}|$ is also shown in Fig. S4(c). The posteriors were obtained by discarding the first 10^4 steps as a burn-in phase. The Metropolis acceptance rate was $\sim 30\%$.

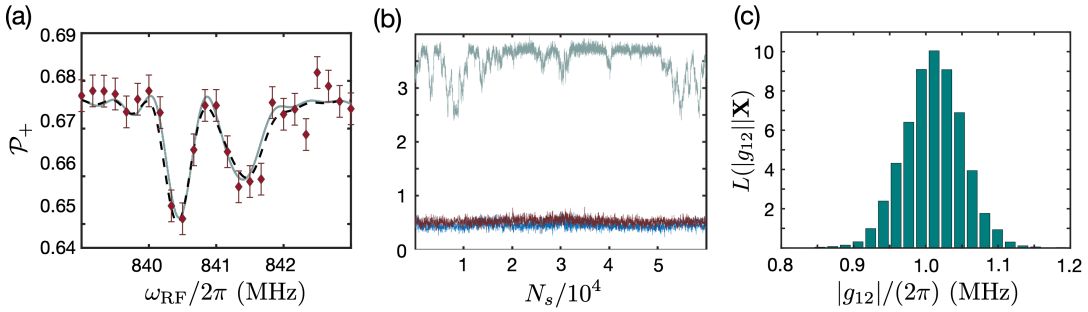

FIG. S4. (a) Simulated experimental dataset $\mathbf{X}$ (red points). The dataset contains $M = 25$ frequencies $\omega_{{\rm RF},j}$ swept across the target nitroxide resonance, with $N_m = 2 \times 10^4$ ideal measurements for each frequency. The error bars are given by $\sigma_m = \sqrt{\left(1 - \overline{\mathcal{S}}^2\right)/4N_m} \approx \sqrt{0.22/N_m}$. The "true" spectrum $\left(\overline{\langle\sigma^x\rangle}_{\rm NV} + 1\right)/2$ (solid line) and the simplified model $\left(\overline{\mathcal{S}}(\omega_{\rm RF}) + 1\right)/2$ (dashed line) are also shown (see text for details about the used parameters). (b) Metropolis Markov chain for the parameters $C_\pm$ (red and blue) and d_{12} (grey). The contrasts $C_\pm$ are dimensionless and are multiplied by 10 for easier viewing. The distance d_{12} is measured in nm. (c) Marginal posterior $L(|g_{12}|\|\mathbf{X})$ obtained from the Markov chain by combining the parameters d_{12}, A_β, and ϕ_β according to $g_{12} = \left(\mu_0\gamma_e^2\hbar/4\pi d_{12}^3\right)\left(1 - 3A_\beta^2\cos^2\phi_\beta\right)$. All samples before $N_s = 10^4$ were discarded. The expectation value is $|g_{12}|/2\pi = 1.010(41)$ MHz, in good agreement with the ideal value $|g_{12}|/2\pi = 1$ MHz. The error is given by the standard deviation of the marginal posterior.

When the measurements are not ideal, preparation of the NV in the $m_S = 0$ state (mapped to $\sigma^x = +1$) leads to a photon detection with probability $p \ll 1$, while preparation of the NV in the $m_S = \pm 1$ state (mapped to $\sigma^x = -1$) leads to no photon detection. Under these assumptions, we estimate that the measurement noise variance scales as $\sigma_m^2 \approx (1 + \overline{\mathcal{S}})/2pN_m$ [S3]. For $\overline{\mathcal{S}} \approx 0.34$ and for an experimentally achievable ground state detection efficiency $p \approx 0.12$ [S4], this gives $\sigma_m^2 \approx 5.6/N_m$. Comparing with the ideal case, we find that the same variance as for ideal measurements is achieved with approximately 25 times more measurements. In the present case, this would require $N_m \approx 5 \times 10^5$ non-ideal measurements per RF frequency. The execution time of the sequence (4.6 μs), plus measurement and reinitialization (~ 3 μs) and some additional time to assure reliable thermalization of the labels ($\sim 3T_1$) leads to a total time of ~ 20 μs per shot. Assuming $M = 25$ inspected frequencies and $N_m \approx 5 \times 10^5$, the experiment would require 250 s to be completed.

[S1] F. Shi, Q. Zhang, P. Wang, H. Sun, J. Wang, X. Rong, M. Chen, C. Ju, F. Reinhard, H. Chen, J. Wrachtrup, J. Wang, and J. Du, Single-protein spin resonance spectroscopy under ambient conditions, Science **347**, 1135 (2015).

[S2] W. R. Gilks, S. Richardson, and D. J. Spiegelhalter, *Markov Chain Monte Carlo in Practice* (Chapman & Hall/CRC, New York, 1996).

[S3] B. D'Anjou and W. Coish, Soft decoding of a qubit readout apparatus, Phys. Rev. Lett. **113**, 230402 (2014), see the Supplemental Material for general expressions for the variance of a non-ideal measurement.

[S4] N. H. Wan, B. J. Shields, D. Kim, S. Mouradian, B. Lienhard, M. Walsh, H. Bakhru, T. Schröder, and D. Englund, Efficient extraction of light from a nitrogen-vacancy center in a diamond parabolic reflector, Nano Lett. **18**, 2787 (2018).